Non-synchronous vibration of a Jeffcott rotor due to internal radial clearance in roller bearings

Jing Wu, Mathias Legrand, Christophe Pierre

To cite this version:

Jing Wu, Mathias Legrand, Christophe Pierre. Non-synchronous vibration of a Jeffcott rotor due to internal radial clearance in roller bearings. 8th IFToMM International Conference on Rotor Dynamics, KIST, Sep 2010, Seoul, South Korea. pp.446-453. hal-00533285

HAL Id: hal-00533285
https://hal.science/hal-00533285v1

Submitted on 5 Nov 2010

Non-synchronous vibration of a Jeffcott rotor due to internal radial clearance in roller bearings

Jing Wu, Master Student
Structural Dynamics and Vibration Laboratory, Department of Mechanical Engineering, McGill University, 817 Sherbrooke St West, Montreal, Quebec H3A 2K6, Canada

Mathias Legrand, Research Associate
Structural Dynamics and Vibration Laboratory, Department of Mechanical Engineering, McGill University, 817 Sherbrooke St West, Montreal, Quebec H3A 2K6, Canada

Christophe Pierre, Professor
Structural Dynamics and Vibration Laboratory, Department of Mechanical Engineering, McGill University, 817 Sherbrooke St West, Montreal, Quebec H3A 2K6, Canada

Abstract

Internal radial clearance (IRC) in roller bearings must be kept to a minimum to avoid non-synchronous vibration (NSV). However, tight IRC increases the risk of bearing durability so that initial clearance is often on the high side and then reduced if necessary when problems with NSV are detected. In rolling element bearings, non-synchronous vibration may be originated by nonlinear contacts, which strongly depend on the IRC. In this paper, instead of the commonly used Hertz contact theory, the Lagrangian multipliers method is adopted to handle the nonlinear contacts between rollers and the outer ring. In order to reduce computational costs, a modal reduction technique is used. The influence of the roller bearing parameters on the NSV is analyzed. Among the existing parameters, the IRC plays the most important role in controlling the NSV.

1 Introduction

Non-synchronous vibration (NSV) in roller bearings is known as an important source of noise in aircraft engines. The frequency range of this NSV is typically in the region which causes cabin comfort issues for mid size business jets (50−200Hz) [1]. Not only the bearing's parameters have effects on the NSV, but also the unbalanced forces added on the shaft play a role in controlling it. [2] analyzed the NSV in rotor bearing system with a flexible shaft and supporting journal bearings. A typical oil-whip phenomenon, which could lead to the failure of the rotor bearing system is analyzed. The oil-whip phenomenon was also studied in [3]. The author studied the influence of imbalance on both the synchronous and non-synchronous vibration based on cascade diagrams for short journal bearings.

One significant source of NSV in rolling element bearings is the nonlinear contact between rollers and the outer ring. The contacts in roller bearings are inherently nonlinear [4]. Bearing contacts have been studied extensively in the past years, and two approaches, namely the classic Hertz contact theory and the Lagrange multipliers method, are widely adopted to handle the contacts in rolling element bearings [5, 6]. The main difference between these two approaches is that the Hertzian contact theory treats the contacts as external forces while the Lagrange multipliers method handles the contact as constraints on the generalized coordinates [7].

Similar to other rotor bearing systems, in our system, the number of linear degrees of freedom is substantial in comparison with that of nonlinear components. However, even though the nonlinear components constitute a small part of the whole degrees of freedom, the system still behaves a nonlinear fashion [8]. In general, the direct way to solve the large order nonlinear dynamic equations is to use direct integration with iteration in time domain. Nevertheless, this method is very computational expensive [9]. In order to improve the computational efficiency,modal reduction techniques are proposed to reduce the system size. Actually, if the number of nonlinear components is very small compared to the whole system, the computational effects will be expected to reduce substantially [10].

In this study, the non-synchronous vibration of a Jeffcott rotor with flexible shaft and two rigid roller bearings is studied. The system excitation force is the unbalanced force added on the central disk. Nonlinearity is due to the nonlinear contact between rollers and the outer ring in the roller bearings. Different from the widely used Hertzian theory, the Lagrange multipliers method compatible with the central difference operator is adopted in solving the contacts [11]. In order to improve the computational efficiency, the Craig-Bampton modal reduction technique is used [12]. In this analysis, the effects of IRC, roller numbers, unbalanced forces on the NSV are analyzed in details, and the relation of largest NSV with respect to the IRC is extracted using curve fitting.

2 Roller bearing model

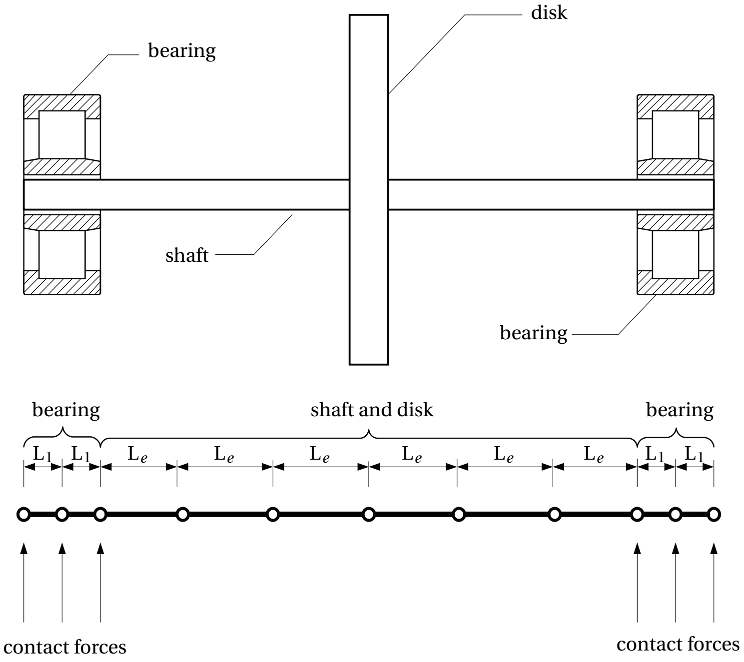

FIGURE 1: Finite element model of the rotor bearing system

In our study, the mathematical rotor bearing system includes two parts: the finite element model of the flexible shaft and the concentrated mass of the central disk. Moreover, at each end of the flexible shaft, supporting forces exist due to the nonlinear contacts in the cylindrical roller bearings. A schematic diagram of the rotor bearing system as well as the cylindrical roller bearing are shown in Fig. 1 and Fig. 2 respectively. The shaft is divided into twenty beam elements, and each node has four degrees of freedom (two translational displacements u_y, u_x, and two rotational deflections θ_y, θ_x).

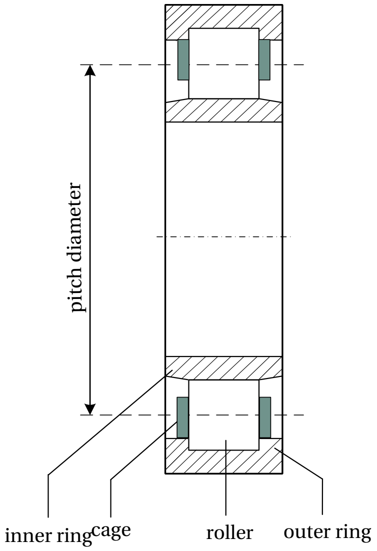

FIGURE 2: Roller bearing of interest

The system's equation of motion is expressed as:

$$\mathbf{M}\ddot{\mathbf{q}} + \mathbf{D}\dot{\mathbf{q}} + \mathbf{K}\mathbf{q} = \mathbf{F}_{\mathrm{un}} + \mathbf{W} + \mathbf{F}_{\mathrm{NL}} \tag{1}$$

where $\mathbf{M} \in \mathbb{R}^{n\times n}$ is the symmetric global mass matrix, $\mathbf{K} \in \mathbb{R}^{n\times n}$ is the symmetric global stiffness matrix, $\mathbf{G}$ is the gyroscopic matrix which is skew-symmetric and $\mathbf{D} = \omega\mathbf{G} + \alpha\mathbf{K} + \beta\mathbf{M}$[1] is the global damping matrix. Vector $\mathbf{F}_{\mathrm{un}} \in \mathbb{R}^n$ stands as the unbalanced force applied on the central disk, $\mathbf{W} \in \mathbb{R}^n$ is the weight of the shaft and $\mathbf{F}_{\mathrm{NL}} \in \mathbb{R}^n$ is the nonlinear contact force vector, due to non-penetration conditions between the cage and the rollers. Finally, $\mathbf{q} \in \mathbb{R}^n$ is the displacement vector and ω is the rotational velocity of the shaft.

The system's excitation force is due to the unbalanced force vector $\mathbf{F}_{\mathrm{un}}$, which is expressed as:

$$\mathbf{F}_{\mathrm{un}} = \begin{pmatrix} me\omega^2\sin(\omega t) \\ me\omega^2\cos(\omega t) \end{pmatrix}$$

where m and e are the unbalanced mass and eccentricity respectively, and ω is the shaft rotational velocity.

The solution of the system's equation of motion is obtained using numerical methods. The explicit Newmark-β integration algorithm is chosen.

3 Modal reduction

Based on the full-order finite element model of the Jeffcott rotor, the simplest way to solve the dynamic equations is direct integration in the time domain. However, this method is very computationally expensive [9]. In general, rotor-bearing systems usually have a very large number of

---

[1] α and β are proportional damping coefficients, $\alpha = 0.005, \beta = 0.01$.

Bearing Parts	Dimension	Value
Inner Ring	Inner Diameter	0.0559 m
	Outer Diameter	0.0665 m
Outer Ring	Inner Diameter	0.0787 m
	Outer Diameter	0.0820 m
Roller	Length/Height	0.0070 m
Bearing	Pitch Diameter	0.0696 m
	IRC	10 µm-120 µm
	Speed Range	1-20000 rpm

TABLE 1: Roller bearing geometry

DOFs while the nonlinear components are spatially localized. Although the nonlinear DOFs only constitute a small part of the whole system, the rotor-bearing system still behaves in a nonlinear fashion [8]. In order to improve the computational efficiency, modal reduction techniques are proposed to reduce the system size.

Direct modal reduction of large mechanical systems can be used to reduce the number of equations of motion by limiting the frequency content of the structure response in a narrow range [10]. Unfortunately, the direct access to physical quantities such as displacement will be lost then making the treatment of the unilateral contact conditions tedious. Accordingly, the chosen strategy is to select a component mode synthesis method that keeps a part of the displacement unknowns (where contact is anticipated and later called nonlinear DOFs) in the reduced-order model.

With its high modal accuracy and capability to reduce the size of dynamic systems, the Craig-Bampton modal reduction technique is chosen in this work. In this method, the DOFs are divided into boundary components and internal components [12]. Hence, partition of the stiffness matrix is denoted as:

$$\begin{pmatrix} \mathbf{F}_\mathrm{B} \\ \mathbf{F}_\mathrm{I} \end{pmatrix} = \begin{bmatrix} \mathbf{K}_\mathrm{BB} & \mathbf{K}_\mathrm{BI} \\ \mathbf{K}_\mathrm{IB} & \mathbf{K}_\mathrm{II} \end{bmatrix} \begin{pmatrix} \mathbf{q}_\mathrm{B} \\ \mathbf{q}_\mathrm{I} \end{pmatrix} \tag{2}$$

where the subscripts B and I denote boundary and internal DOFs, $\mathbf{q}_\mathrm{B}$ and $\mathbf{q}_\mathrm{I}$ are the boundary and internal displacement vectors. According to [12], the constraint modes are defined as the mode shapes of the internal DOFs due to successive unit displacement of the boundary points, with all other boundary points totally constrained. Hence, the constraint modes are obtained by the assumption that forces add on the internal DOFs are equivalent to 0, i.e.:

$$\mathbf{0} = \mathbf{K}_\mathrm{IB}\mathbf{q}_\mathrm{B} + \mathbf{K}_\mathrm{II}\mathbf{q}_\mathrm{I} \tag{3}$$

Equation (3) can be written in a simple form as:

$$\mathbf{q}_\mathrm{I} = -\mathbf{K}_\mathrm{II}^{-1}\mathbf{K}_\mathrm{IB}\mathbf{q}_\mathrm{B} = \mathbf{\Phi}_c\mathbf{q}_\mathrm{B} \tag{4}$$

where $\mathbf{\Phi}_c$ is the so-called matrix of constraint modes.

Similarly, the mass matrix is partitioned as:

$$\bar{\mathbf{M}} = \begin{bmatrix} \mathbf{M}_\mathrm{BB} & \mathbf{M}_\mathrm{BI} \\ \mathbf{M}_\mathrm{IB} & \mathbf{M}_\mathrm{II} \end{bmatrix} \tag{5}$$

The eigenvectors of the internal DOFs are the normal modes of the constraint substructure. Therefore, the following equation is obtained:

$$\omega^2\mathbf{M}_\mathrm{II}\boldsymbol{\phi}_\mathrm{I} = \mathbf{K}_\mathrm{II}\boldsymbol{\phi}_\mathrm{I} \tag{6}$$

in which each column of the eigenvector $\boldsymbol{\phi}_{\mathrm{I}}$ forms the respective column of normal modes matrix $\boldsymbol{\Phi}_{\mathrm{N}}$. Let the reduction matrix be partitioned as:

$$\boldsymbol{\Phi} = [\boldsymbol{\Phi}_{\mathrm{C}}\ \boldsymbol{\Phi}_{\mathrm{N}}] \tag{7}$$

Defining a set of modal coordinates $\mathbf{u}$ which includes the constraint and fixed-interface modes of the system, and it is divided as:

$$\mathbf{u} = \begin{pmatrix} \mathbf{u}_{\eta} \\ \mathbf{u}_{\mathrm{I}} \end{pmatrix} \tag{8}$$

where the subscript η refers to constraint modes.

With reference to [12], the coordinate transformation matrix $\boldsymbol{\Psi}$ is written as:

$$\boldsymbol{\Psi} = \begin{bmatrix} \mathbf{I} & \mathbf{0} \\ \boldsymbol{\Phi}_c & \boldsymbol{\Phi}_{\mathrm{N}} \end{bmatrix} \tag{9}$$

such as:

$$\mathbf{q} = \boldsymbol{\Psi}\mathbf{u} \tag{10}$$

where the mass, damping and stiffness matrices of the reduced-order model are:

$$\tilde{\mathbf{M}} = \boldsymbol{\Psi}^{\mathrm{T}}\bar{\mathbf{M}}\boldsymbol{\Psi}, \qquad \tilde{\mathbf{K}} = \boldsymbol{\Psi}^{\mathrm{T}}\bar{\mathbf{K}}\boldsymbol{\Psi} \tag{11}$$

Also, the reduced-order proportional damping matrix $\tilde{\mathbf{D}}$ is:

$$\tilde{\mathbf{D}} = \alpha\tilde{\mathbf{M}} + \beta\tilde{\mathbf{K}} \tag{12}$$

Three criteria, namely eigenvalue plots, displacement response and frequency response, are applied to analyze the performance of the proposed Craig-Bampton modal reduction technique. On the basis of the reduction process, the size of our system is significantly reduced while the reduced-order model can capture most of the nonlinear response of the system.

4 Contacts in roller bearings

4.1 Hertzian contact model

There has been a lot of interest in the modeling of contacts in rolling element bearings in the past years. In fact, the physical modeling of the bearing contacts is a complex task which depends on the rotational velocity, contact geometry, materials of contact surface, internal radial clearance, etc [9]. In general, the contacts between rollers and the outer ring are handled by the widely used Hertzian theory. In the classic Hertzian theory, the contact involves estimation of the contact stiffness and the penetration depth of rollers to the outer ring at the contact line. However, in many cases, the estimation of the contact stiffness and the penetration depth is extremely difficult due to the fact that they are sensitive to complex operating conditions [13].

In Hertzian theory, the nonlinear contact forces are introduced as a function of the contact stiffness K and contact damping C acting on the penetration depth h_j at the contact line for the j^{th} roller [5]. The penetration depth h_j is introduced as the interaction of the j^{th} roller with the outer ring at the contact line when the roller comes in the loading zone as shown in Fig. 3. Distance h_j is expressed as:

$$h_j = u_y \sin\theta_j + u_x \cos\theta_j - \gamma_0 \tag{13}$$

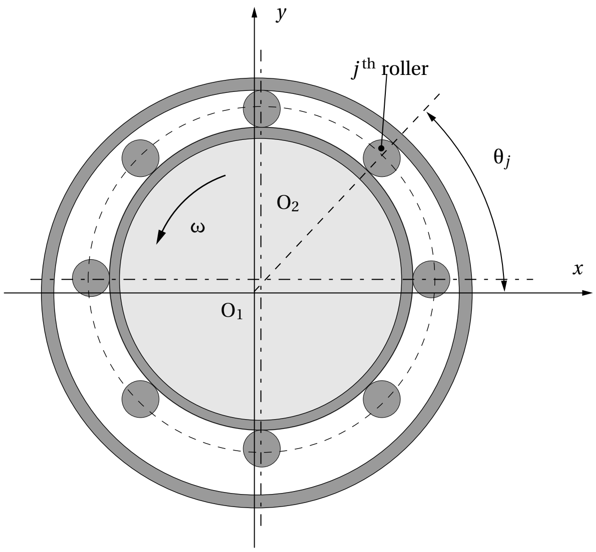

FIGURE 3: Bearing Contact Model

where u_y and u_x are the vertical and horizontal displacement of the rotor respectively, and θ_j is the angular position of the j^{th} roller, γ_0 is the initial internal radial clearance[2]. Therefore, the contact force is estimated as:

$$\mathbf{F}_{\text{NL}} = \begin{cases} \text{K}h_j + \text{C}\dot{h}_j, & \text{if} \quad h_j \geq 0 \\ 0, & \text{if} \quad h_j < 0 \end{cases}$$

where K and C are the contact stiffness and damping coefficients, respectively.

4.2 Lagrange multipliers method

Alternatively, another approach which is based on the Lagrange multipliers method is developed to account for contacts between rollers and the outer ring. This Lagrangian approach avoids direct modeling of the contact forces and thus avoids the limitations of the Hertzian theory. In the Lagrangian method, the contact forces are treated as constraints on the generalized coordinates on the basis of Lagrange multipliers and hence, they are calculated automatically at each time step [6]. In other words, during the integration of the system's equation of motion, the contact forces are calculated automatically at the cost of more unknowns.

For the Jeffcott model, the shaft is supported by the nonlinear contact forces in two roller bearings at its ends. For each roller bearing, contact occurs when the radial displacement of the rotor consumes the initial internal radial clearance. According to Lagrangian method, the outer ring of the bearing constrains the rotor's radial displacement. Thus, the motion of the rotor is constrained by the following equations for each roller bearing:

$$\begin{aligned} h_{1j} &= u_{y1}\sin\theta_j + u_{x1}\cos\theta_j - \gamma_0 \\ h_{2j} &= u_{y2}\sin\theta_j + u_{x1}\cos\theta_j - \gamma_0 \end{aligned} \tag{14}$$

where u_{y1}, u_{x1} and u_{y2}, u_{x2} are the vertical and horizontal displacement of the rotor at each bearing location, respectively.

---

[2] γ_0 is the air gap between the rotating shaft and the outer ring, which is defined as the initial internal radial clearance

By incorporating equation (14) into the system's equation of motion (1), we obtain:

$$\mathbf{M}\ddot{\mathbf{q}}+\mathbf{J}^{\mathrm{T}}\lambda+(\mathbf{D}+\omega\mathbf{G})\dot{\mathbf{q}}+\mathbf{K}\mathbf{q}=\mathbf{F} \tag{15}$$

where **F** is the external force vector, which includes unbalanced forces, gravity and nonlinear contact forces. The Lagrange multiplier vector λ may be written as:

$$\lambda=\begin{pmatrix}\lambda 1_1 & \lambda 1_2 & \dots & \lambda 1_{\mathrm{N}_b} & \lambda 2_1 & \lambda 2_2 & \dots & \lambda 2_{\mathrm{N}_b}\end{pmatrix}^{\mathrm{T}} \tag{16}$$

$\lambda 1_j$ and $\lambda 2_j$ are Lagrange multipliers for the j^{th} constraint at each roller bearing, respectively. In equation (15), **J** is the contact matrix (Jacobian matrix) whose j^{th} row is the partial derivative of the j^{th} constraint equation with respect to the generalized coordinates. For each bearing, the number of rollers defines the number of constraint equations. Hence, the contact matrix is expressed as:

$$\mathbf{J}=\begin{bmatrix}\sin\theta_1 & \cos\theta_1 & 0 & \cdots & 0 & 0 & 0 & 0 & 0\\ \sin\theta_2 & \cos\theta_2 & 0 & \cdots & 0 & 0 & 0 & 0 & 0\\ \vdots & & & & & & & & \vdots\\ \sin\theta_{\mathrm{N}_b} & \cos\theta_{\mathrm{N}_b} & 0 & \dots & 0 & 0 & 0 & 0 & 0\\ 0 & 0 & 0 & \cdots & 0 & \sin\theta_1 & \cos\theta_1 & 0 & 0\\ 0 & 0 & 0 & \cdots & 0 & \sin\theta_2 & \cos\theta_2 & 0 & 0\\ \vdots & & & & & & & & \vdots\\ 0 & 0 & 0 & \cdots & 0 & \sin\theta_{\mathrm{N}_b} & \cos\theta_{\mathrm{N}_b} & 0 & 0\end{bmatrix} \tag{17}$$

As explained before, the contact forces are determined on the basis of the Lagrange multiplier vector λ:

$$\mathbf{F}_{\mathrm{NL}}=-\mathbf{J}^{\mathrm{T}}\lambda \tag{18}$$

The contact forces should be negative during each contact period to maintain the motion of rotor within the inner surface of the outer ring. If a positive contact force is detected, the algorithm automatically switches to the non-contact configuration.

As mentioned before, the explicit Newmark-β method is adopted to solve the system's equations of motion. Hence, the Lagrange multipliers method compatible with the Newmark-β method is used to handle the contacts in our system. The algorithm includes three parts:

1. **Resetting initial conditions —** The initial conditions are first set for the $n+1$ time step. Involving mass, damping and stiffness matrix **M**, **D** and **K**, the resetting of the initial displacement vector is (with subscript r for resetting):

$$\mathbf{q}_{n+1,r}=\left[\frac{\mathbf{M}}{h^2}+\frac{\mathbf{D}}{2h}\right]^{-1}\left(\left(\frac{2\mathbf{M}}{h^2}-\mathbf{K}\right)\mathbf{q}_n+\left(\frac{\mathbf{D}}{2h}-\frac{\mathbf{M}}{h^2}\right)\mathbf{q}_{n-1}+\mathbf{F}_n\right) \tag{19}$$

2. **Computation of contacts —** From the contact matrix (Jacobian matrix) **J**, the clearance distances are stored as:

$$\mathbf{g}_{n+1}=\mathbf{J}^{\mathrm{T}}\mathbf{q}-\gamma_0 \tag{20}$$

where γ_0 stands as initial uniform clearance.

3. **Correction —** The correction should be considered for each time step. For the determination term g_{n+1}, only the positive terms are chosen, the negative terms are treated 0, which means that the determination terms are kept only when the contact occurs. The correction term yields the additional equations for the unknown Lagrange multipliers vector λ,

$$\mathbf{q}_{n+1}=\mathbf{q}_{n+1,s}-\left[\frac{\mathbf{M}}{h^2}+\frac{\mathbf{D}}{2h}\right]^{-1}\mathbf{J}^{\mathrm{T}}\lambda \tag{21}$$

From equations (19), (20) and (21), the Lagrange multiplier vector is obtained as:

$$\lambda=\left(\mathbf{J}\left[\frac{\mathbf{M}}{h^2}+\frac{\mathbf{D}}{2h}\right]^{-1}\mathbf{J}^{\mathrm{T}}\right)^{-1}\mathbf{g}_{n+1} \tag{22}$$

5 Results and discussion

5.1 Case studies

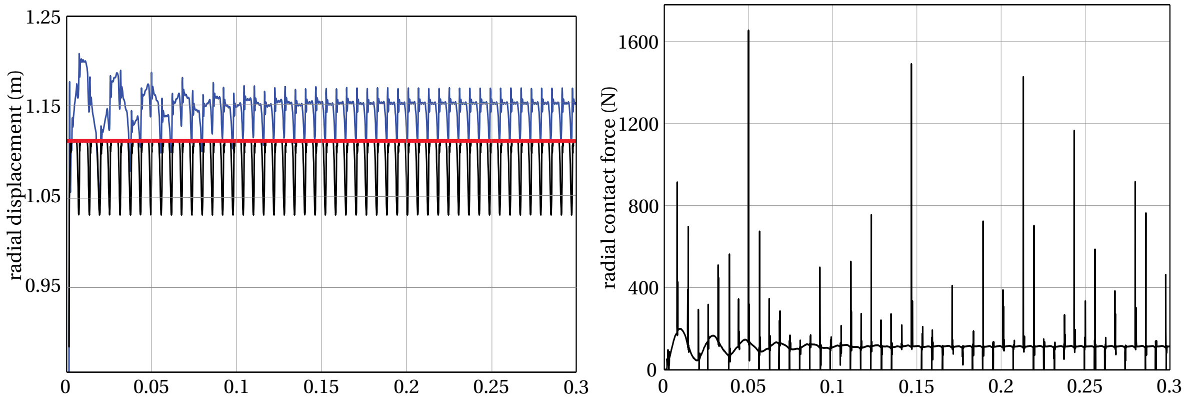

(a) time response (— Hertz theory; — Lagrange multipliers method; — radial clearance)

(b) contact force

FIGURE 4: Responses through Lagrange multipliers method at $\omega = 50$ Hz and $\gamma_0 = 10$ µm

Through the Newmark-β method, the vibratory responses of the rotor are investigated. Two cases are investigated via this constraint Lagrange multipliers approach. For both cases, the rotor's radial displacement responses are compared with that using Hertz approach. Also, the bearing's contact force for each case is analyzed.

Fig. 4 illustrates the rotor's displacement response at the bearing location and the bearing radial contact force ($\omega = 50$ Hz and $\gamma_0 = 10$ µm). Under low radial clearance (10 µm), the radial displacement responses obtained via the Hertz approach and Lagrange multipliers method are shown in Fig. 4(a). It is apparent that for Lagrange multipliers approach, rollers move back simultaneously when they consume the internal radial clearance. At the same time, contact occurs and no residual penetration is observed. Conversely, for Hertz contact, rollers continue to move into the outer ring even though they consume the internal radial clearance completely as displayed in Fig. 4(a). It is also noticeable that the penetration depth is very small compared to the internal radial clearance. If we look at the contact force shown in Fig. 4(b), it is interesting to see that peaks appear when the rollers contact the outer ring.

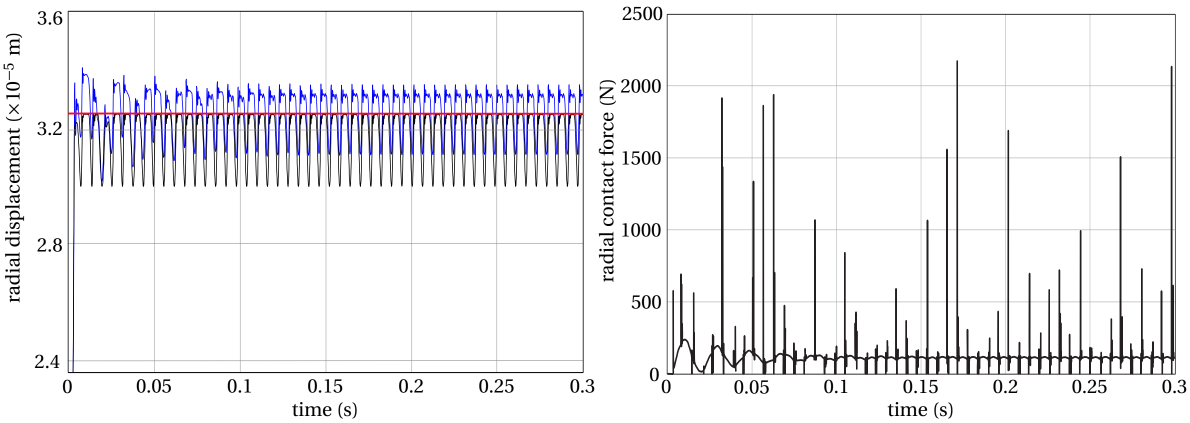

(a) time response (— Hertz theory; — Lagrange multipliers method; — radial clearance)

(b) contact force

FIGURE 5: Responses through Lagrange multipliers method at $\omega = 50$ Hz and $\gamma_0 = 30$ µm

As the internal radial clearance is increased to 30 µm, the rotor response and bearing radial contact force are shown in Figs. 5(a) and 5(b), respectively. Penetration is detected through the Hertz approach; while for the Lagrange multipliers method, the rotor maximum radial displacement is equivalent to the internal radial clearance. With the increase of internal clearance, both the radial displacement and contact force increase.

5.2 Non-synchronous vibration analysis

Analysis of the non-synchronous vibration sensitivity to roller's parameters is the main objective of this work. In the introduced roller bearing model, the frequency range of the non-synchronous vibration lies in the region causing cabin comfort issues for mid size business jets (50-200 Hz). Accordingly, it is of primary interest to determine the key parameters controlling the non-synchronous vibration. The effects of the internal radial clearance (IRC), the number of rollers (N_b) and the mass imbalance threshold (me) are investigated within the frameworks of the Lagrange multipliers method. The cascade diagram is adopted to observe the dynamic behaviors of the rotor due to nonlinear contact forces in the frequency domain. This cascade diagram is constructed through fast Fourier transform of periodic responses of the disk at different rotational velocities. It can correlate the signal magnitude, rotational velocity and frequency spectrum, in order to illustrate whether synchronous vibration, non-synchronous vibration or even both dominate the precessional vibration [14]. The largest non-synchronous vibration with respect to the internal radial clearance is also studied.

5.2.1 Sensitivity to internal radial clearance

Through the Lagrange multipliers method, the non-synchronous vibration with respect to the internal radial clearance is illustrated in Fig. 6. Analogous to the frequency responses through the Hertz approach, the non-synchronous vibration becomes much more significant with the increase of the internal clearance. Similarly, under higher internal clearance, the resonance in the synchronous vibration moves slightly to lower frequency (about 51 Hz). This is due to the fact that the natural frequencies of the system depend on the internal radial clearance, which could be investigated through nonlinear normal modes.

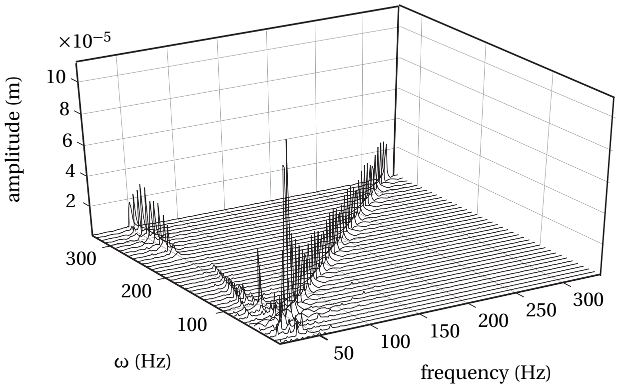

(a) $\gamma_0 = 20\ \mu\text{m}$

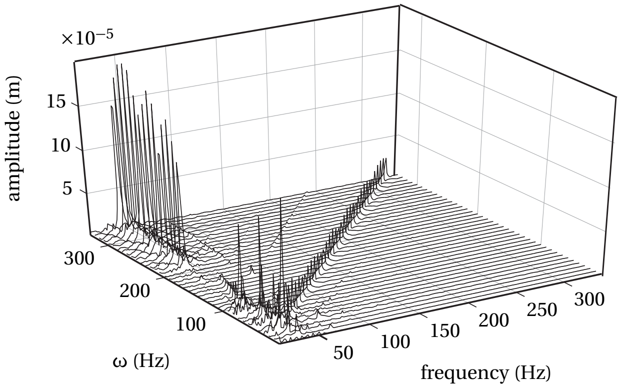

(b) $\gamma_0 = 60\ \mu\text{m}$

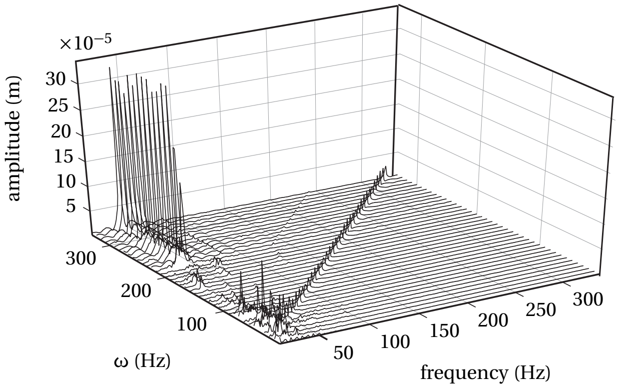

(c) $\gamma_0 = 120\ \mu\text{m}$

FIGURE 6: cascade diagram under effects of the IRC (N_b and $me = 4 \times 10^{-5}$ m)

With $N_b = 8$ and $me = 4 \times 10^{-5}$ m, the frequency responses in the framework of cascade diagrams are illustrated in Fig. 6. As shown in Fig. 6(a), the synchronous vibration dominates in the frequency response. At $\omega = 51$ Hz, which is also the first critical speed, the resonance appears in the synchronous vibration. At higher velocity ($\omega = 100$ Hz), a sub-synchronous vibration appears. This sub-synchronous vibration is called *whirl phenomenon* and arises at twice the first critical speed [3]. Compared to the resonance response, the sub-synchronous vibration is small. As the velocity keeps growing close to the second critical speed ($\omega = 251$ Hz), the *whip phenomenon* emerges. This whip phenomenon is related to the rotor lateral forward precessional subharmonic vibration around the bearing center [2]. The whip has a constant frequency not depending on the rotational velocity. Moreover, in the frequency axis, the whip phenomenon occurs close to the first natural frequency of the rotor-bearing system, which is the so-called *frequency-locked phenomenon* [15]. In general, the whip does not vary with the rotational velocity and locks close to the first resonance of the rotor [14]. The amplitude of the whip is higher than that of the whirl; however, in comparison with the synchronous vibration, the whip is not dominant.

The cascade diagrams with $\gamma_0 = 60$ µm and $\gamma_0 = 120$ µm are shown in Figs. 6(b) and 6(c), respectively. In comparison with the results where $\gamma_0 = 20$ µm, both the whirl and whip vibration grow significantly. If we look at the cascade diagram under $\gamma_0 = 60$ µm (Fig. 6(b)), it is apparent that instead of only synchronous vibration, a combination of the synchronous and non-synchronous vibration begins to dominate in the precessional vibration. If the internal radial clearance keeps increasing, the non-synchronous vibration becomes dominant (Fig. 6(c)). The largest amplitude of the non-synchronous vibration is about ten times of that under $\gamma_0 = 20$ µm. Resonance still occurs close to the first natural frequency in the synchronous vibration; however, the synchronous vibration does not increase with the internal radial clearance. It is also noticeable to see that with larger internal radial clearance, the onset of the non-synchronous vibration moves towards lower rotational velocity.

5.2.2 Sensitivity to mass imbalance

After the analysis of the effect of the internal radial clearance, numerous simulations are conducted to study the effect of mass imbalance ($me = 1 \times 10^{-5}$ m; $me = 2 \times 10^{-5}$ m; and $me = 4 \times 10^{-5}$ m) on the non-synchronous vibration.

With $N_b = 8$ and $\gamma_0 = 20$ µm, the frequency responses with respect to the mass imbalance are illustrated in Fig. 7. For a low mass eccentricity ($me = 1 \times 10^{-5}$ m), it is apparent that only the synchronous vibration dominates in the precessional vibration and the non-synchronous vibration is negligible (Fig. 7(a)). If the mass eccentricity is increased to 2×10^{-5} m, the synchronous vibration increases, and the non-synchronous vibration is still negligible (Fig. 7(b)). Nevertheless, the non-synchronous vibration increases significantly with a further increase of the mass eccentricity (Fig. 7(c)). With $me = 4 \times 10^{-5}$ m, the synchronous vibration is no longer the only vibration in the cascade diagram. Although the non-synchronous vibration is still small in comparison with the synchronous vibration, it is not negligible. It is also noticeable to see that the sub-synchronous whirl phenomenon appears at $\omega = 100$ Hz, and its amplitude is the same as that of the whip phenomenon.

5.2.3 Sensitivity to number of rollers

The non-synchronous vibration with respect to the number of rollers ($N_b = 8$; $N_b = 16$; and $N_b = 32$) is now studied.

For $\gamma_0 = 20$ µm and $me = 4 \times 10^{-5}$ m, the frequency responses of the disk with respect to the number of rollers are illustrated in the cascade diagrams in Fig. 8. The number of rollers does not have an significant effect on the non-synchronous vibration. The onset of the non-synchronous whip is close to $\omega = 250$ Hz, and the amplitude is about 3×10^{-5} m. Besides, the sub-synchronous whirl also appears at twice the first critical speed. It is noticeable that for all configurations, the synchronous vibration dominates in the frequency response. In general, in comparison with internal radial clearance and mass imbalance, the number of rollers plays little on the non-synchronous vibration.

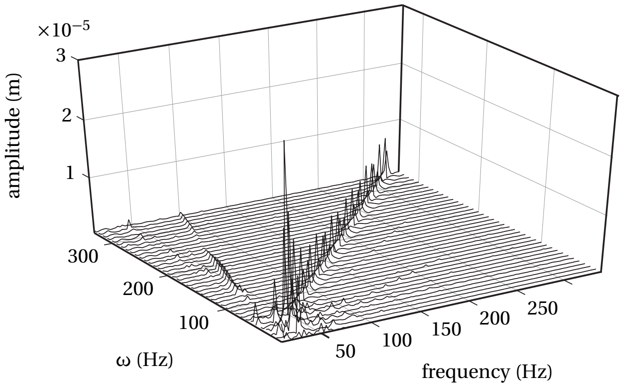

(a) $me = 1 \times 10^{-5}$ m

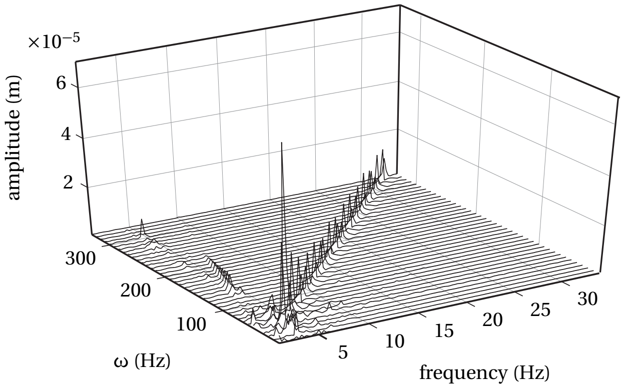

(b) $me = 2 \times 10^{-5}$ m

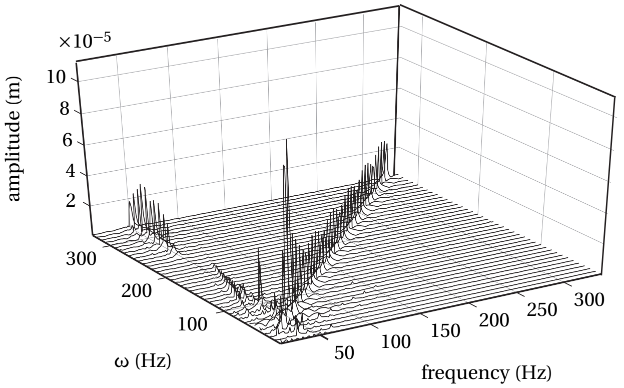

(c) $me = 4 \times 10^{-5}$ m

FIGURE 7: cascade diagram under effects of the mass imbalance ($N_b = 8$ and $\gamma_0 = 20$ μm)

5.3 Largest Non-synchronous Vibration with IRC

In engineering applications, the non-synchronous vibration is one important source of the failure of rotor-bearing systems [16]. Since the internal radial clearance plays the most significant role in controlling the NSV, it makes sense to obtain the relationship of the largest NSV with respect to the internal radial clearance. This relationship is possible to predict dangerous behaviors of the system with respect to the internal clearance.

From above analysis, the largest amplitude of the NSV is invariant with solution methods adopted. By means of the Lagrange multipliers method, the largest NSV with respect to the internal radial clearance is illustrated in Fig. 9 ($N_b = 8$ and $me = 4 \times 10^{-5}$ m). It can be seen that the largest

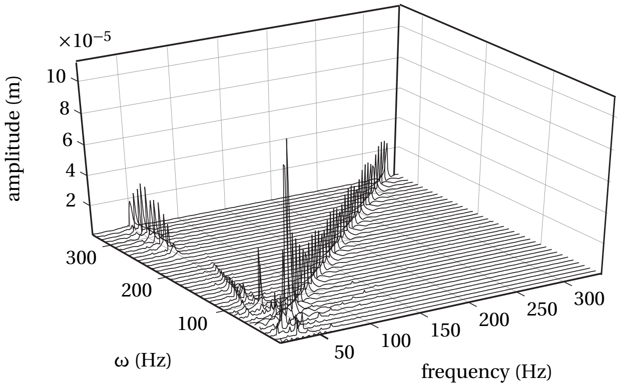

(a) $N_b = 8$

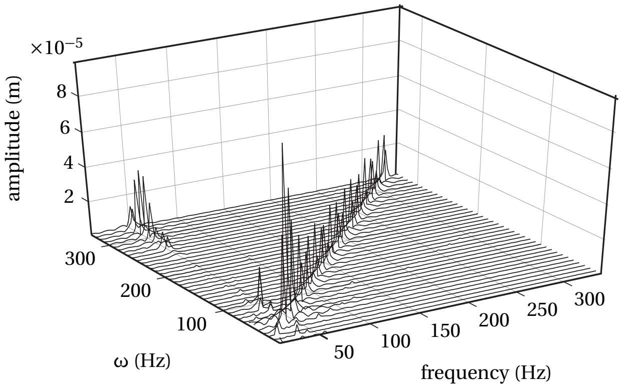

(b) $N_b = 16$

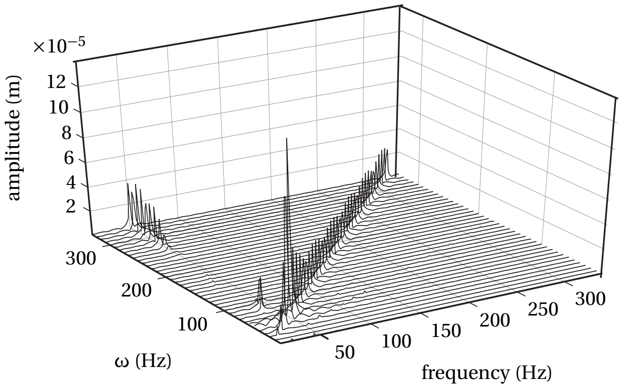

(c) $N_b = 32$

FIGURE 8: cascade diagram under effects of the roller numbers ($\gamma_0 = 20$ µm and $me = 4 \times 10^{-5}$ m)

NSV obeys a nonlinear relation with the internal radial clearance. Following [17], the curve fitting technique is used to formulate their relationship as:

$$\delta_{nsv} = P_1\gamma^3 + P_2\gamma^2 + P_3\gamma + P_4 \tag{23}$$

where δ_{nsv} is the largest NSV, $P_i\,(i = 1, \ldots, 4)$ are the fitted coefficients, γ is the internal radial clearance. The curve fitting coefficients are listed in Table 2.

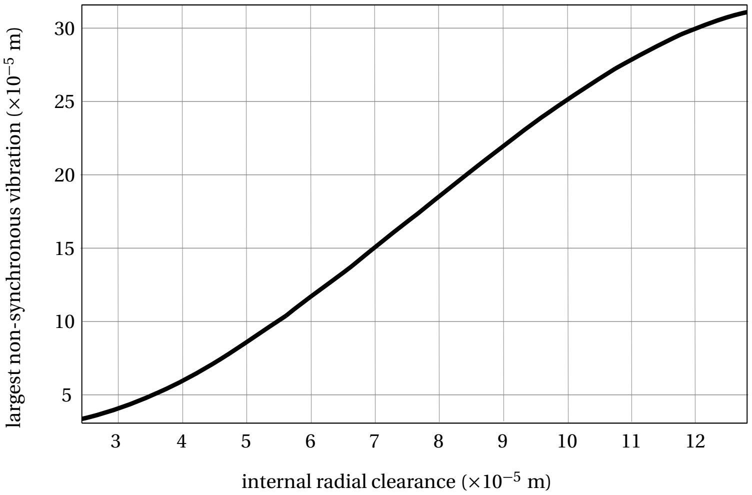

FIGURE 9: Largest non-synchronous vibration with respect to IRC ($me = 4 \times 10^{-5}$ m and $N_b = 8$)

Coefficient	Values
P_1	-3.125×10^8
P_2	7.162×10^4
P_3	-1.956
P_4	4.296×10^{-5}

TABLE 2: Curve fitting coefficients for the largest non-synchronous vibration

6 Conclusions

In this paper, the effects of different parameters of roller bearings on the non-synchronous vibration is analyzed. Unlike the commonly used Hertzian theory, the Lagrange multipliers compatible with explicit central difference method is adopted to handle the nonlinear contacts in the roller bearing. Time history of the system response is chosen to compare the Lagrange multipliers technique and the Hertz contact method. As predicted, penetration between contact targets is found to be a noticeable difference between these two techniques. Generally, rotor-bearing systems are very computationally expensive and the nonlinear DOFs are spatially localized. In order to improve computational efficiency, the Craig-Bampton modal reduction technique is used to reduce the size of the system. System responses obtained by the reduced-order model are compared with that by the full-order model and match well, while at the same time, the CPU time is significantly reduced. Through Fast Fourier Transforms of the system responses, the non-synchronous vibration with respect to the bearing's parameters can be studied in the frequency domain. Among all existing parameters, the internal radial clearance is found to play the most important role in controlling the non-synchronous vibration. Moreover, since the clearance is significant in the nature of the non-synchronous vibration, the largest non-synchronous vibration with respect to the clearance is also analyzed to predict possible failures of the system.

References

[1] P. . Whitney, *Pratt & Whitney Project Description*, Pratt & Whitney, 2008.

[2] J. Jing, G. Meng, S. Xia, *On the Oil-Whipping of a Rotor-Bearing System by a Continuum Model*,

Applied Mathematical Modelling 29 (2005) 461–475.
http://dx.doi.org/10.1016/j.apm.2004.09.003

[3] H. Castro, K. Cavalca, R. Nordmann, *Whirl and Whip Instabilities in Rotor-Bearing System Considering a Nonlinear Force Model*, Journal of Sound and Vibration 317 (2008) 273–293.
http://dx.doi.org/10.1016/j.jsv.2008.02.047

[4] B. Changqing, X. Qingyu, *Dynamic Model of Ball Bearings with Internal Clearance and Waviness*, Journal of Sound and Vibration 294 (1-2) (2006) 23–48.
http://dx.doi.org/10.1016/j.jsv.2005.10.005

[5] M. Tiwari, K. Gupta, *Effect of Radial Internal Clearance of a Ball Bearing on the Dynamics of a Balanced Horizontal Rotor*, Journal of Sound and Vibration 238 (2000) 723–756.
http://dx.doi.org/10.1006/jsvi.1999.3109

[6] M. Sahinkaya, A. Abulrub, P. Keogh, C. Burrows, *Multiple Sliding and Rolling Contact Dynamics for a Flexible Rotor/Magnetic Bearing System*, IEEE/ASME Transactions on Mechatronics 12 (2007) 179–189.

[7] S. Harsha, *Nonlinear Dynamic Analysis of a High-speed Rotor Supported on Rolling Element Bearings*, Journal of Sound and Vibration 29.
http://dx.doi.org/10.1016/j.jsv.2005.03.008

[8] Z. Qu, *Model Reduction for Dynamical Systems with Local Nonlinearities*, AIAA Journal 40 (2002) 327–333.
http://dx.doi.org/10.2514/2.1649

[9] T. Harris, M. Kotzalas, *Advanced Concepts of Bearing Technology*, Taylor & Francis, 2006.

[10] R. Guyan, *Reduction of Stiffness and Mass Matrices*, AIAA Journal 3 (2) (1965) 380.
http://dx.doi.org/10.2514/3.2874

[11] N. Carpenter, R. Taylor, M. Katona, *Lagrange constraints for transient finite element surface contact*, International Journal for Numerical Methods in Engineering 32 (1991) 123–128.
http://dx.doi.org/10.1002/nme.1620320107

[12] R. Craig, M. Bampton, *Coupling of Substructures for Dynamic Analysis*, AIAA Journal 6 (7) (1968) 1313–1319.

[13] T. Harris, *Rolling Bearing Analysis*, John Wiley and Sons, 2001.

[14] J. JianPing, M. Guang, S. Yi, X. SongBo, *On the non-linear dynamic behavior of a rotor-bearing system*, Journal of Sound and Vibration 274 (3-5) (2004) 1031–1044.
http://dx.doi.org/10.1016/S0022-460X(03)00663-1

[15] A. Muszynska, *Whirl and whip rotor/bearing stability problems*, Journal of Sound and Vibration 110 (1986) 443–462.
http://dx.doi.org/10.1016/S0022-460X(86)80146-8

[16] S. Crandall, *From whirl to whip in rotordynamics*, in: 3rd IFToMM Conference on Rotordynamics, Lyon, France, 1990, pp. 19–26.

[17] D. Fleming, B. Murphy, J. Sawicki, J. Poplawski, *Transient Response of Rotor on Rolling Element Bearings with Clearance*, in: 7th IFToMM Conference on Rotordynamics, Vienna, Austria, 25-28 September 2006.